

1 **Line of Sight Displacement from ALOS-2 Interferometry: Mw 7.8**
2 **Gorkha Earthquake and Mw 7.3 Aftershock**

3

4 Eric O. Lindsey¹

5 Ryo Natsuaki²

6 Xiaohua Xu¹

7 Masanobu Shimada²

8 Manabu, Hashimoto³

9 Diego Melgar⁴

10 David T. Sandwell¹

11

12 ¹Institute for Geophysics and Planetary Physics, University of California, San Diego,
13 USA

14 ²Earth Observation Research Center, Japan Aerospace Exploration Agency (JAXA),
15 Tsukuba, Japan

16 ³Disaster Prevention Research Institute, Kyoto University, Kyoto, Japan

17 ⁴Seismological Laboratory, UC Berkeley, Berkeley, USA

18

19 **Key Points**

20 Observations of the Mw 7.8 Gorkha, Nepal earthquake and Mw 7.3 aftershock are
21 presented.

22 ALOS-2 provides burst-aligned ScanSAR interferometry with 350 km swath width.

23 Data from co- and post-seismic interferograms are available online for use in modeling
24 studies.

25

26 **Abstract**

27 Interferometric Synthetic Aperture Radar (InSAR) is a key tool for the analysis of
28 displacement and stress changes caused by large crustal earthquakes, particularly in
29 remote areas. A challenge for traditional InSAR has been its limited spatial and temporal
30 coverage especially for very large events, whose dimensions exceed the typical swath
31 width of 70 – 100 km. This problem is addressed by the ALOS-2 satellite, whose
32 PALSAR-2 instrument operates in ScanSAR mode, enabling a repeat time of 2 weeks
33 and a swath width of 350km. Here, we present InSAR line-of-sight displacement data
34 from ALOS-2/PALSAR-2 observations covering the Mw 7.8 Gorkha, Nepal earthquake
35 and its Mw 7.3 aftershock that were acquired within one week of each event. The data
36 are made freely available and we encourage their use in models of the fault slip and
37 associated stress changes. The Mw 7.3 aftershock extended the rupture area of the
38 mainshock toward the east, but also left a 20 km gap where the fault has little or no co-
39 seismic slip. We estimate this un-slipped fault patch has the potential to generate a Mw
40 6.9 event.

41

42 **Keywords**

43 ScanSAR interferometry, ALOS-2, PALSAR-2, InSAR, Gorkha Earthquake, Nepal

44

45 **Index Terms**

46 1209 Tectonic Deformation

47 1240 Satellite geodesy: results

48 1241 Satellite geodesy: technical issues

49

50 **1. Introduction**

51 The Mw 7.8 Gorkha, Nepal earthquake and Mw 7.3 aftershock struck in a region with
52 less than optimal seismic and geodetic coverage [e.g. Ader et al., 2012]. The moment
53 tensor solution based on far-field seismic stations combined with the tectonics of the
54 region suggests thrust faulting on a shallow dipping fault (11°) having a strike of 295°
55 [USGS, 2015]. Initial finite fault models based on methods of *Ji et al.*, [2002] show 2-4
56 m of slip at ~ 15 km depth over a zone extending ~ 150 km ESE of the hypocenter. The
57 earthquake caused intense ground shaking throughout much of Nepal and parts of India
58 and China, resulting in over 8,000 deaths. Ground shaking in the Kathmandu basin was
59 particularly intense as a result of its proximity to the main rupture area and the effects of
60 basin amplification and directivity, causing many historical structures to collapse that had
61 survived previous earthquakes [USGS, 2015].

62 Several Interferometric Synthetic Aperture Radar (InSAR) satellites were operational
63 at the time of the earthquake and continue to collect measurements of line-of-sight (LOS)
64 displacement. The Sentinel-1a satellite, operated by the European Space Agency (ESA)
65 collected C-band InSAR observations, which were processed and made available online
66 by the ESA Scientific Exploitation of Operational Missions project (SEOM -
67 <http://insarap.org>). The ALOS-2 satellite, operated by the Japan Aerospace Exploration
68 Agency (JAXA), collected L-band InSAR data, low-resolution images of which are
69 presented at the JAXA site (<http://www.eorc.jaxa.jp/ALOS/en/>) as well as the Geospatial
70 Information Authority of Japan (GSI - [http://www.gsi.go.jp/cais/topic150429-index-
71 e.html](http://www.gsi.go.jp/cais/topic150429-index-e.html)).

72 This study is focused on the extraction of LOS displacement from the ALOS-
73 2/PALSAR-2 instrument, with the objective to provide these observations to the
74 modeling community, as the raw data are not freely available and this is the first
75 publication of ALOS-2 ScanSAR InSAR. Rapid assessment of the acquired data is also
76 important for scheduling of future acquisitions. ALOS-2 operates in several modes,
77 including traditional strip-mode SAR with a swath width of 70km, and ScanSAR (Wide
78 Swath), with a width of 350km. Although wide swath is data is desirable, most
79 interferograms are constructed from strip-mode data and ScanSAR-to-ScanSAR
80 interferometry is rare because it requires accurate burst alignment between the reference
81 and repeat orbit. This implies precise on-board timing to better than 70 milliseconds.

82 This was first achieved with the ALOS-1 satellite in cases where the bursts were aligned
83 by chance [Tong *et al.*, 2008]. ALOS-2 is the first L-band satellite to offer burst-aligned
84 ScanSAR interferometry as a standard operating mode, but during the commissioning of
85 the satellite it was discovered that the burst alignment was inconsistent. The problem was
86 corrected on February 8 2015, 11 weeks prior to the M7.8 rupture and thus the quality of
87 the ScanSAR interferograms was not completely understood at the time of the mainshock.
88 Below, we demonstrate that the burst alignment problem was indeed corrected; a more
89 detailed analysis of the issue is included in Appendix A. ScanSAR-to-ScanSAR
90 interferograms (Figure 1) provide an accurate and complete mapping of the surface
91 displacement of these two major earthquakes, which occurred in a region with the
92 greatest topographic relief on Earth.

93 This manuscript describes the new data and processing methods and more importantly
94 refers to a web site where we present line-of-sight (LOS) data files for each track and
95 frame described here. We will continue to provide post-seismic LOS data as they become
96 available. The data were processed with an updated version of GMTSAR software
97 [Sandwell *et al.*, 2011] with additional post processing using GMT [Wessel *et al.*, 2013]
98 and SNAPHU [Chen and Zebker, 2000]. The details of the processing are described in
99 Appendix B. The results show continuous phase across the subswath boundaries and
100 demonstrate that the PALSAR-2 radar provides spatially consistent phase over the entire
101 region (Figure 1).

102

103 **2. Line of Sight Displacement**

104 ALOS-2 InSAR coverage of the Mw 7.8 and Mw 7.3 ruptures is excellent. Each
105 rupture was independently imaged from both the ascending and descending look
106 directions (Figures 2 and 3). Coherence is maintained except in areas of very steep
107 topography or snow cover. A close inspection of the mainshock interferograms (Figures
108 2a and 3a) shows no major discontinuities in phase near the surface trace of the Main
109 Himalayan Thrust (MHT). Indeed the surface displacement field is smooth and
110 consistent with the majority of slip occurring between 10 and 20 km depth, with virtually
111 all slip to the East of the hypocenter. Since the LOS vector from the descending pass
112 (Path 48) is nearly parallel to the strike of the MHT, the LOS motion primarily reflects

113 vertical deformation caused by a large amount of slip on a shallow dipping fault. In
114 contrast, the LOS vector from the ascending pass (Path 157) is at about a 30° angle from
115 the strike of the fault so it records a larger LOS displacement (Figure 3a). Preliminary
116 modeling (below) suggests that the maximum fault slip lies between the maximum and
117 minimum lobes in the LOS displacement, at a depth of about 15 km.

118 The LOS displacement from the Mw 7.3 aftershock shows a pattern that is similar, but
119 more compact, than the displacement from the mainshock (Figure 2b, 3b). As in the case
120 of the mainshock, the trough-to-peak displacement of the aftershock is larger along the
121 ascending track than it is along the descending track, in agreement with a slip vector
122 oriented along dip. The low-to-high gradient in the displacement of the aftershock is
123 larger than the mainshock suggesting there is a slip concentration at depth. Most of the
124 displacement from the Mw 7.3 aftershock occurs near the eastern end of the displacement
125 from the main rupture suggesting it may have been triggered by a Coulomb stress
126 concentration from the mainshock.

127 To better understand how the surface displacements relate to slip at depth, we inverted
128 the LOS displacements for descending and ascending tracks for both mainshock and
129 aftershock. We used the 1D layered Earth structure and inversion method of *Melgar &*
130 *Bock* [2015]. We assume a planar fault derived from the nodal plane of a W-phase
131 moment tensor inversion [USGS, 2015] with a strike of 295° and a dip of 11° . For the
132 mainshock we discretized the dislocation surface into 10×10 km subfaults, and for the
133 aftershock into 5×5 km subfaults. The LOS measurements are down-sampled using the
134 QuadTree technique [Lohman & Simons, 2005]; the distribution of down-sampled data
135 and residuals are shown in Figure S1. The inverse problem is ill-posed, so the inversion is
136 regularized by applying minimum norm smoothing. The regularization parameter, which
137 limits the level of roughness, is objectively selected by using Akaike's Bayesian
138 Information Criterion [Yabuki & Matsu'Ura, 1992]. We assume uniform uncertainties for
139 the InSAR data, which therefore do not affect the regularization. We consider the effect
140 of inverting for slip using only the descending or ascending tracks individually in Figure
141 S2, and the effect of choosing a higher or lower penalty on the model norm (greater or
142 lesser smoothing) in Figure S3.

143 The results are shown in Figure 2d. Mainshock slip extends over an area ~170 km long
144 and between the 5 to 15 km depth contours, with peak slip of 5.5 – 6.5 m over a large
145 asperity just north of Kathmandu. Peak slip depends somewhat on the choice of
146 regularization; see Figure S3. Peak slip for the aftershock may be slightly larger but is
147 less well constrained (5.5 – 10 m, depending on the regularization) and is concentrated on
148 a very compact asperity about 30 km in length. The aftershock slip area shows little to no
149 overlap with the mainshock slip. Notably, there is an area of little or no slip at 15-20 km
150 depth between the two events. This gap appears to be well constrained by the data
151 irrespective of the value of the regularization parameter (Figure S3).

152

153 **3. Discussion and Conclusions**

154 The displacement field for the interferogram and derived slip inversions spanning both
155 the mainshock and aftershock show an interesting pattern. While the aftershock extended
156 the rupture area of the mainshock toward the east, it did not completely fill the “gap”
157 formed by the NE trending tongue in high slip. Thus, a large (20 km) area remains where
158 the fault has little or no co-seismic slip (Figure 2d). By scaling the area of the
159 displacement field from the Mw 7.3 rupture to the area of the un-ruptured zone, we
160 estimate this un-slipped fault patch has the potential to generate a Mw 6.9 event.
161 Furthermore, the tongue of surface displacement maps to a smaller asperity in the
162 mainshock slip pattern at 20-25 km depth. If this represents the down dip edge of the
163 seismogenic zone, then there is potential for further slip down dip of the patches broken
164 thus far. It will be important to monitor this slip gap over the coming years, a task that
165 will be aided by the recently-installed continuous GPS site GUMB [*John Galetzka,*
166 *personal communication, 2015*]. If ALOS-2 continues operating in the ScanSAR mode
167 along path 048 with a 14 to 42-day repeat, it will be possible to acquire a complete space-
168 time map of this and other regions surrounding the rupture zone.

169 The ScanSAR InSAR capabilities of ALOS-2 prove to be a capable tool for
170 monitoring large continental earthquakes such as the Nepal sequence. The Himalayan
171 region has the largest relief on the Earth, is densely vegetated, and has snow-capped
172 peaks. The L-band radar enables adequate InSAR correlation in the vegetated areas,
173 while tight baseline control of the spacecraft to better than 120 m in these examples

174 minimizes the unwanted phase due to errors in the extreme topography. Finally, the
175 onboard navigation is now accurate enough to provide better than 70% overlap of the
176 ScanSAR bursts between reference and repeat images. This results in single
177 interferograms 350 km wide that are able to completely image the deformation resulting
178 from these major events. This wide swath also enables a short 14-day repeat interval that
179 was able to collect images between the Mw 7.8 and Mw 7.3 events. Slip models based
180 on the deformation spanning the Mw 7.8 event can be used to estimate the Coulomb
181 stress that may have triggered the Mw 7.3 event. The slip gap observed between the two
182 ruptures (Figure 2d) can now be monitored for co-seismic slip or aseismic creep. Finally,
183 the large vertical displacement caused by this thrust event will also induce significant
184 viscoelastic deformation over the next years to decades that we hope will be accurately
185 imaged and modeled.

186

187 **Appendix A. Burst Alignment**

188 ALOS-2 is the first L-band SAR with routine InSAR acquisitions in the ScanSAR
189 mode [Kankaku *et al.*, 2009]. The interferometric wide mode (WD1) has 5 subswaths to
190 achieve an overall ground swath width of 350 km, with characteristics provided in Table
191 S1. The wide swath makes it possible to completely image an area every 14 days instead
192 of the 42-day repeat interval that is needed for complete imaging in swath mode. There
193 are two basic requirements for achieving accurate displacement maps from normal strip-
194 mode InSAR. First the along-track Doppler spectra of the reference and repeat images
195 should have more than about 50% overlap. Second, the perpendicular baseline distance
196 between the reference and repeat acquisitions should be smaller than about 20% of the
197 critical baseline. ALOS-2 is well within these limits so one can construct high quality
198 strip-mode interferograms from all the acquisitions. However, construction of high
199 quality ScanSAR to ScanSAR interferograms also requires that the bursts have more than
200 50% overlap on the ground. Poor quality interferograms can be achieved when the burst
201 overlap is as small as 20%.

202 To achieve this burst overlap the radar system must be triggered with an along-track
203 accuracy better than ~500m, which corresponds to a timing accuracy better than 70
204 milliseconds [Tong *et al.*, 2010]. The autonomous navigation system aboard ALOS-2

205 was designed to achieve horizontal baseline better than 500 m and along-track accuracy
 206 of 10 m [Kankaku *et al.*, 2009]. During the commissioning phase of the mission, accurate
 207 baseline control was demonstrated with most perpendicular baselines less than 200 m.
 208 However the initial interferograms usually had no burst overlap. JAXA implemented an
 209 adjustment to the onboard navigation system in early February 2015 and adequate burst
 210 overlap has been maintained since then. The first pass after the February 8 fix and prior
 211 to the Nepal earthquakes was P048 on February 22. Subsequent pairs have burst overlap
 212 better than 70%, as listed in Table A1.

213 We performed a systematic analysis of the burst overlap between acquisitions from
 214 before and after February 8, 2015 for ten different locations worldwide, the results of
 215 which are listed in Table S2. We found an approximately 365-day sinusoidal oscillation
 216 in the burst overlap (Figure A1). The amplitude of the oscillation is greater than the 2100-
 217 pixel burst spacing, so the values are wrapped onto the range (-1050, 1050). We fit a
 218 model of the form:

$$219$$

$$220 \quad B(D) = \text{mod} \left\{ A \sin \left[2\pi (D - D_0) / T \right] + 1050, 2100 \right\} - 1050 \quad (\text{A1})$$

221

222 where B is the burst offset at day D , in days relative to date D_0 . The best-fitting
 223 parameters are amplitude $A = 3635$ pixels, period $T = 365$ days, and zero phase date $D_0 =$
 224 December 20, 2014.

225 Equation A1 can be used to predict interferometric pairs that are likely to have better
 226 than 20% burst overlap. In Figure A1, the dark grey box centered at 0 burst offset shows
 227 the dates of acquisitions with a 95% chance of more than 20% burst overlap with
 228 acquisitions after February 8. The corresponding date ranges are July 22 – July 31,
 229 November 8 – November 17, December 16 – December 23, and January 20 – January 29.
 230 The lighter grey box centered at a burst offset of -900 shows an example of acquisitions
 231 that will correlate with each other but not with acquisitions after February 8.

232

233 **Appendix B. InSAR processing and Phase Unwrapping**

234 The ALOS-2 PALSAR-2 data were processed using an updated version of the
 235 GMTSAR software [Sandwell *et al.*, 2011] and the phase was unwrapped using

236 SNAPHU software [Chen & Zebker, 2000]. Interferograms used are given in Table A1.
237 In all cases we started with the Single Look Complex (SLC, L1.1) products with HH
238 polarization, in CEOS format as delivered from the AUIG User Interface Gateway
239 (<https://auig2.jaxa.jp/ips/home>). For the ScanSAR processing we began with the full
240 aperture product. The ScanSAR interferograms were low-pass filtered with a 0.5 gain at
241 500 m wavelength while a 200-m low-pass filter was applied to the strip-mode data. Our
242 strategy is to process each frame (along-track) or subswath (across-track) independently
243 in radar coordinates and assemble them in geographic coordinates. We have found that
244 phase will be nearly continuous across subswath boundaries if an identical orbit and
245 geometric model is used for all the components [Tong *et al.*, 2010]. The small phase
246 mismatch at the boundaries depends on the method used to align the reference and repeat
247 images. The geometric and orbital errors should only introduce an offset and stretch in
248 both the range and azimuth coordinates, which corresponds to estimating 4 parameters
249 when fitting the sub-window cross correlation peaks. Because of ionospheric distortions
250 in azimuth, we also solve for an additional parameter that corresponds to the stretch in
251 azimuth as a function of azimuth, resulting in a 5-parameter model. If 6 or more
252 parameters are used, the coherence of the interferogram will increase slightly but the
253 phase will have a significant mismatch on frame or subswath boundaries.

254 We unwrapped each frame or subswath independently in radar coordinates using
255 SNAPHU software [Chen & Zebker, 2000] with an improved algorithm for masking of
256 decorrelated areas [Agram and Zebker, 2009]. We then geocoded the results and
257 combined the sub-swaths into a single interferogram by adding a multiple of 2π to
258 achieve matching phase at the boundaries. For several of the subswaths there was also a
259 phase discontinuity across the snow-covered Himalaya Mountains. Again a multiple of 2
260 π was added to the area of discontinuous phase to bring it into accordance with the
261 multi-subswath interferogram. After correcting the integer unwrapping errors, the frames
262 or subswaths were combined using the GMT function `grdblend`, which provides seamless
263 blending in overlap areas. The final unwrapped phase was converted to line-of-sight
264 (LOS) displacement using the appropriate center wavelength. Several of the
265 interferograms have large phase ramps related to orbit error and/or ionospheric delays.
266 We remove a ramp from the composite LOS data by estimating a gradient far from the

267 earthquake displacement; LOS data with no trend removed are also provided. Data are
268 median filtered onto 1km posting and are provided in an ASCII file containing: longitude,
269 latitude, elevation, look vector, LOS (mm) and uncertainty. In addition, the GMT-format
270 NetCDF grid files of geolocated LOS displacements and satellite look vectors at 90-m
271 posting are also available. All results are available at <http://topex.ucsd.edu/nepal> and will
272 be archived at UNAVCO.

273

274 **Acknowledgements**

275 We thank JAXA for rapid acquisition and distribution of the ScanSAR data especially
276 along track 048. The data were provided under PI investigations 1148: Geometric and
277 Interferometric CALVAL of ALOS-2 PALSAR and 1413: Unraveling present-day
278 deformation around the eastern and western syntaxes of the Himalayan range. The
279 development of the GMTSAR software and the ALOS-2 pre-processor was supported by
280 ConocoPhillips and the National Science Foundation through the Geoinformatics
281 program (EAR-1347204) and the GeoEarthScope program (EAR-1147435).

282

283 **References**

- 284 Ader, T., J. P. Avouac, J. Liu-Zeng, H. Lyon-Caen, L. Bollinger, J. Galetzka, J. Genrich,
285 M. Thomas, K. Chanard, S. N. Sapkota, S. Rajaure, P. Shrestha, L. Ding, M. Flouzat
286 (2012), Convergence rate across the Nepal Himalaya and interseismic coupling on the
287 Main Himalayan Thrust: Implications for seismic hazard. *J. Geophys. Res. Solid Earth*
288 117, doi:10.1029/2011jb009071.
- 289
290 Agram, P. S. and H. A. Zebker (2009), Sparse Two-Dimensional Phase Unwrapping
291 Using Regular-Grid Methods, *IEEE Trans. Geosci. Rem. Sensing* Vol. 6, No. 2, pp. 327-
292 331, doi:10.1109/LGRS.2009.2012445.
- 293
294 Bertran-Ortiz, A., and H.A. Zebker (2007), ScanSAR-to-Stripmap Mode Interferometry
295 Processing Using ENVISAT/ASAR Data, *IEEE Trans. Geosci. Rem. Sensing*, Vol. 45,
296 No. 11, pp. 3468-3480, doi:10.1109/TGRS.2007.895970.
- 297
298 Chen C. W. and H. A. Zebker (2000), Network approaches to two-dimensional phase
299 unwrapping: intractability and two new algorithms, *J. Opt. Soc. Am. A*, vol. 17, pp. 401-
300 414 doi:10.1364/JOSAA.17.000401.
- 301
302 Kankaku, Y., Osawa, Y., Suzuki, S., & Watanabe, T. (2009, August). The overview of
303 the L-band SAR onboard ALOS-2. In Proceedings of Progress in Electromagnetics
304 Research Symposium, Moscow.
- 305
306 Lohman, R. B., & Simons, M. (2005). Some thoughts on the use of InSAR data to
307 constrain models of surface deformation: Noise structure and data
308 downsampling. *Geochemistry, Geophysics, Geosystems*, 6(1).
- 309
310 Melgar, D., and Y. Bock (2015), Kinematic earthquake source inversion and tsunami
311 runup prediction with regional geophysical data, *J. Geophys. Res. Solid Earth*, 120,
312 doi:10.1002/2014JB011832.
- 313
314 Sandwell, D. T., R. Mellors, X. Tong, M. Wei, and P. Wessel (2011), Open radar
315 interferometry software for mapping surface deformation, *Eos Trans. AGU*, 92(28), 234,
316 doi:10.1029/2011EO280002.
- 317
318 Tong, X., D. T. Sandwell, and Y. Fialko (2010), Coseismic slip model of the 2008
319 Wenchuan earthquake derived from joint inversion of interferometric synthetic aperture
320 radar, GPS, and field data, *J. Geophys. Res.*, 115, B04314, doi:10.1029/2009JB006625.
- 321
322 USGS event page, <http://earthquake.usgs.gov/earthquakes/eventpage/us20002926>.
- 323
324 Wessel, P., W. H. F. Smith, R. Scharroo, J. F. Luis, and F. Wobbe (2013), Generic
325 Mapping Tools: Improved version released, *EOS Trans. AGU*, 94, 409-410,
326 doi:10.1002/2013EO450001.
- 327

328 Yabuki, T., & Matsu'Ura, M. (1992). Geodetic data inversion using a Bayesian
329 information criterion for spatial distribution of fault slip. *Geophysical Journal*
330 *International*, 109(2), 363-375.
331
332

Track Mode	Reference Date Product	Repeat Date Product	B. perp. (m)	Az. shift (pixel)	Burst overlap	Mean coherence
T048 ScanSAR	FEB 22 2015 ALOS2040533050-150222	APR 05 2015 ALOS2046743050-150405	43.7	-18	95%	0.33
T048 ScanSAR	FEB 22 2015 ALOS2040533050-150222	MAY 03 2015 ALOS2050883050-150503	48.0	-106	72%	0.20
T048 ScanSAR	APR 05 2015 ALOS2046743050-150405	MAY 03 2015 ALOS2050883050-150503	4.3	-84	78%	0.27
T048 ScanSAR	MAY 03 2015 ALOS2050883050-150503	MAY 17 2015 ALOS2052953050-150517	-97.7	3	99%	0.43
T047 ScanSAR	MAR 31 2015 ALOS2046003050-150331	APR 28 2015 ALOS2050143050-150428	81.0	-91	76%	0.25
T157 Swath	FEB 21 2015 ALOS2040460540-150221	MAY 02 2105 ALOS2050810540-150502	-118.6	-3	N/A	0.23
T156 Swath	APR 27 2015 ALOS2050070550-150427	MAY 25 2015 ALOS2054210550-150525	-39.9	-2	N/A	0.29

333

334

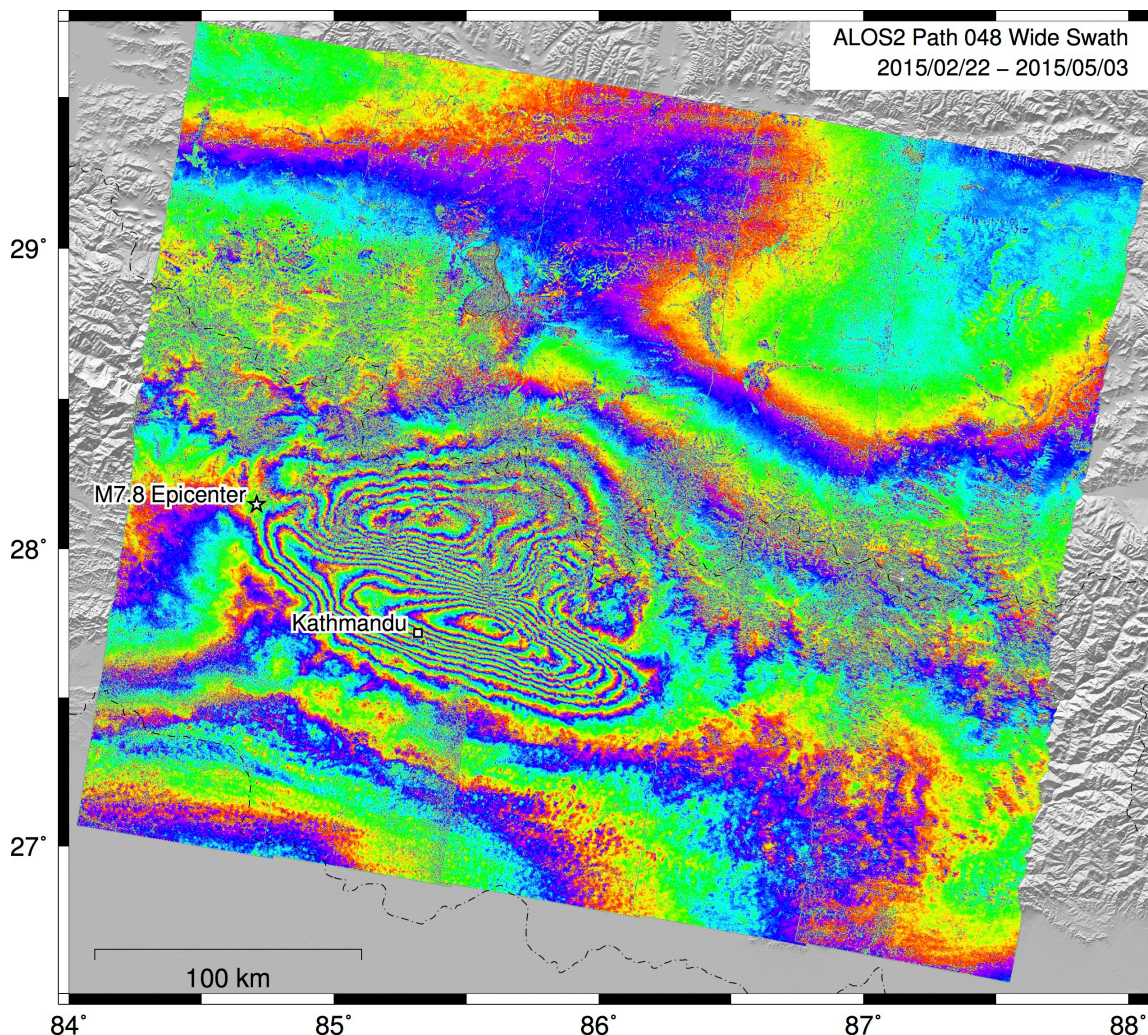
Table A1. Interferograms used in this study. ScanSAR burst overlap is computed

335

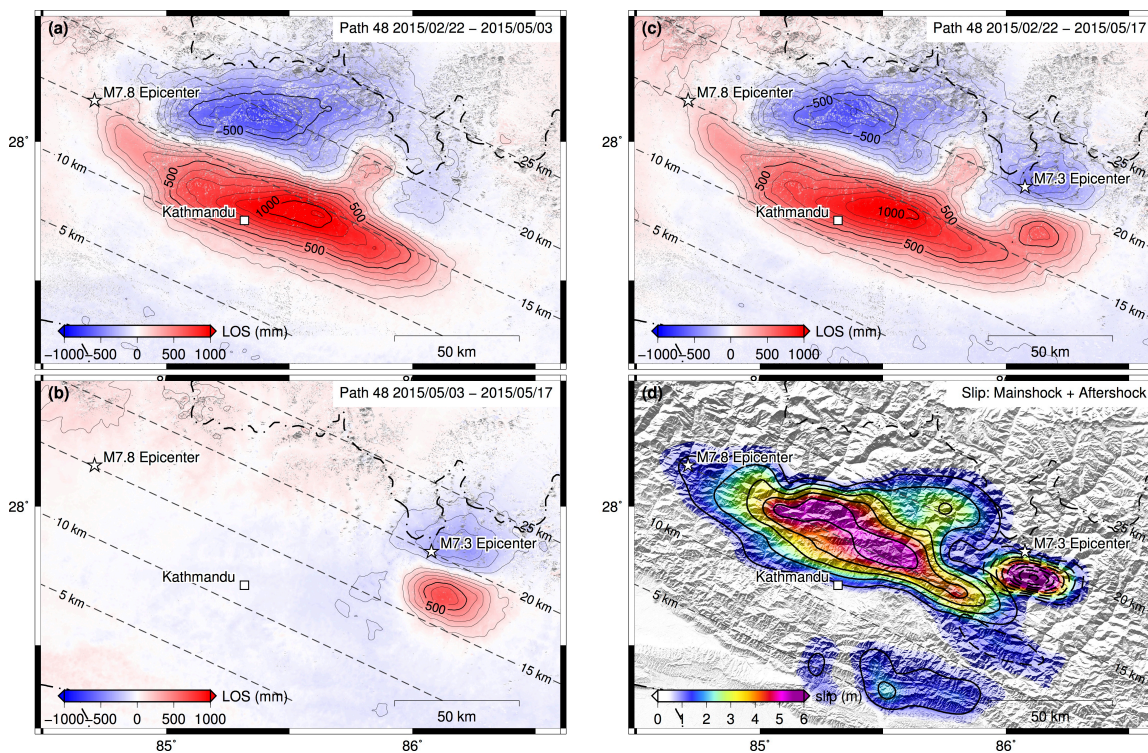
according to the formula $100 * (\text{nburst} - \text{az. shift}) / \text{nburst}$, using nburst for subswath 3 from

336

Table S1.



337 84° 85° 86° 87° 88°
 338 **Figure 1.** Example of a coseismic ScanSAR-to-ScanSAR interferogram from ALOS-2
 339 descending Path 48, spanning dates February 22, 2015 to May 3, 2015 and covering the
 340 Mw 7.8 Gorkha, Nepal earthquake. Each color cycle (red-green-blue-red) represents 12.1
 341 cm of displacement toward the satellite. Data were processed using GMTSAR [*Sandwell*
 342 *et al.*, 2011]. Note ALOS-2 provides continuous phase across subswath boundaries with
 343 no adjustment resulting in a single 350 km by 350 km interferogram.



344

345

346

347

348

349

350

351

352

353

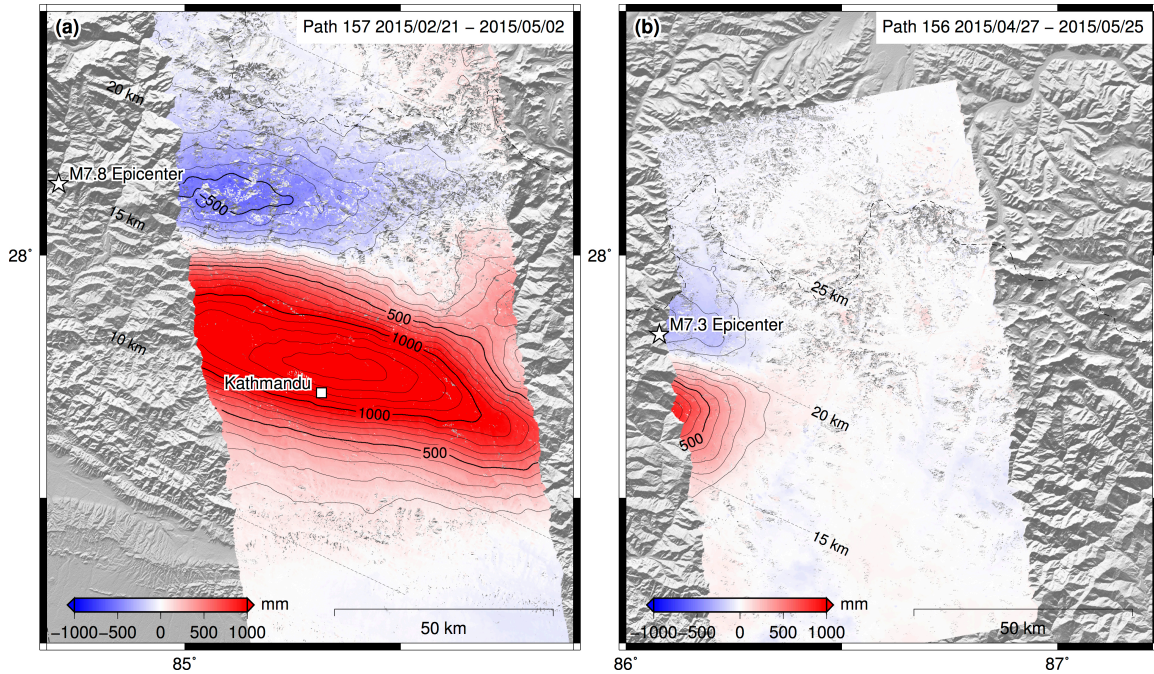
354

355

356

357

Figure 2. LOS displacement in millimeters for sub-area covered by ALOS-2 along descending Path 48. Dashed lines show depth to fault plane, from the USGS W-phase moment tensor solution nodal plane [USGS, 2015]. (a) LOS displacement for a time interval spanning the Mw 7.8 earthquake. This represents mainly vertical motion with a trough-to-peak amplitude of ~ 1.6 m. (b) LOS displacement for a time interval spanning the Mw 7.3 aftershock. The trough-to-peak amplitude is ~ 1.1 m. (c) LOS displacement for a time interval spanning both events. The overall extent of the combined rupture is ~ 170 km. (d) Slip inversion of the LOS data from Paths 48 and 157 based on the modeling approach of *Melgar & Bock* [2015]. Maximum slip is ~ 6 m. The shallow (< 10 km) slip feature is preferred by data from Path 157 but does not appear to be required by the Path 48 data (see Figures S2 and S3). There is a notable gap in slip centered approximately 20 km to the west of the Mw 7.3 aftershock hypocenter.



358

359

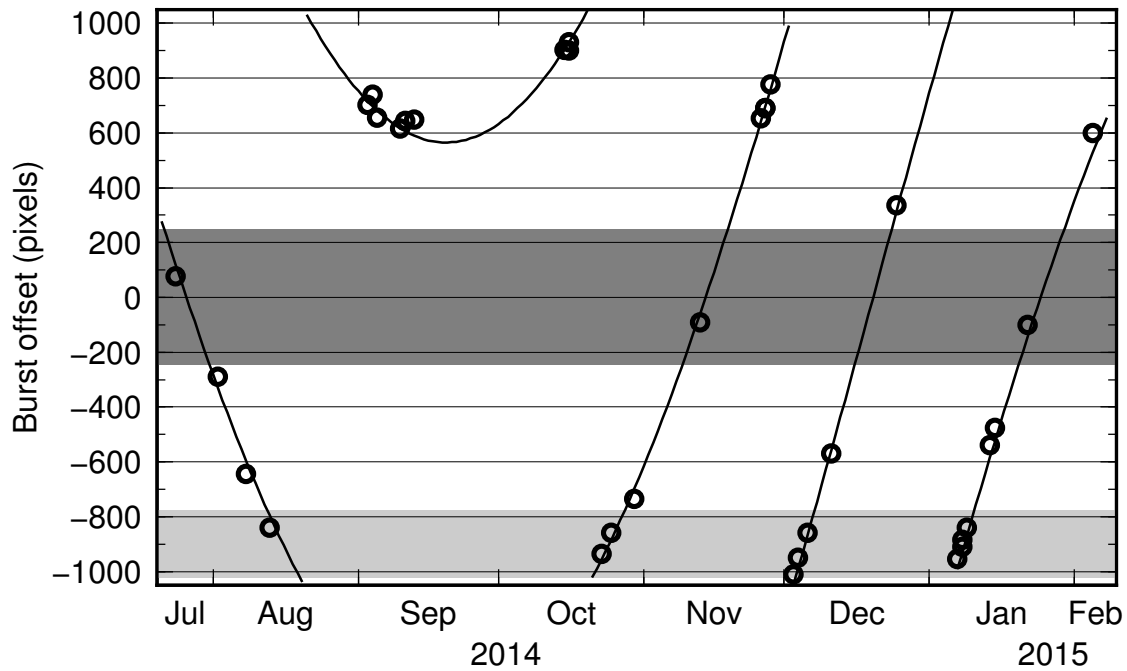
360 **Figure 3.** LOS displacement in millimeters from ALOS-2 along ascending paths.

361 Dashed lines show depth to fault plane. (a) LOS displacement on path 157 spanning the

362 Mw 7.8 earthquake has a trough-to-peak displacement of ~ 2.1 m. (b) LOS displacement363 on path 156 spanning the Mw 7.3 earthquake has a trough-to-peak displacement of ~ 1.1 m.

364

365



366

367

368

369

370

371

372

373

374

Figure A1. Burst offset versus time for subswath 1. Other subswaths follow the same pattern with a different y-axis scale. Circles are the observed burst offset between pre- and post-February 8, 2015 acquisitions at ten different locations worldwide (values are provided in Table S2). The modeled curve was computed using equation A1. Dark grey box shows acquisitions that have a 95% chance of at least 20% burst overlap with post-February 8 data. Lighter grey box shows some example acquisitions that have at least 20% burst overlap only with each other.